Remnant black hole properties from numerical-relativity-informed perturbation theory and implications for waveform modeling

Tousif Islam,[1,2,3,*] Scott E. Field,[2,3] and Gaurav Khanna[4,1,3]

[1]*Department of Physics, University of Massachusetts, Dartmouth, Massachusetts 02747, USA*
[2]*Department of Mathematics, University of Massachusetts, Dartmouth, Massachusetts 02747, USA*
[3]*Center for Scientific Computing and Visualization Research, University of Massachusetts, Dartmouth, Massachusetts 02747, USA*
[4]*Department of Physics and Center for Computational Research, University of Rhode Island, Kingston, Rhode Island 02881, USA*

(Received 20 January 2023; accepted 5 September 2023; published 25 September 2023)

During binary black hole (BBH) mergers, energy and momenta are carried away from the binary system as gravitational radiation. Access to the radiated energy and momenta allows us to predict the properties of the remnant black hole. We develop a Python package `gw_remnant` to extract the remnant mass, remnant spin, peak luminosity, and the final kick imparted on the remnant black hole from the gravitational waveforms. Using this package, we extract the remnant properties of the final black hole in case of nonspinning BBH mergers with mass ratios ranging from $q = 2.5$ to $q = 1000$ using waveform modes generated from `BHPTNRSur1dq1e4`, a recently developed numerical-relativity-informed surrogate model based on the black hole perturbation theory framework. We validate our results against the remnant properties estimated from numerical relativity (NR) surrogate models in the comparable mass-ratio regime and against recently available high-mass-ratio NR simulations at $q = [15, 32, 64]$. We find that our remnant property estimates computed from fluxes at future null infinity closely match the estimates obtained from the NR surrogate model of apparent horizon data. Using Gaussian process regression fitting methods, we train a surrogate model, `BHPTNR_Remnant`, for the properties of the remnant black hole arising from BBH mergers with mass ratios from $q = 2.5$ to $q = 1000$. Finally, we discuss potential improvements in the `BHPTNRSur1dq1e4` waveform model when including remnant information. We make both the `gw_remnant` and `BHPTNR_Remnant` packages publicly available.

DOI: 10.1103/PhysRevD.108.064048

I. INTRODUCTION

During the coalescence, binary black holes (BBHs) dissipate energy, linear momentum, and angular momentum through gravitational radiation. As the system emits energy and angular momentum, the orbit of the binary shrinks, resulting in an inspiral and an eventual merger. At the time of the merger, black holes typically radiate a significant portion of their energy, making a BBH coalescence one of the most luminous events in the Universe [1]. The radiated energy corresponds to a mass deficit in the final black hole (often termed the remnant black hole), while loss of angular momentum impacts the spin of the final black hole [2]. While gravitational radiation will always carry away energy and angular momenta, the binary must have some degree of asymmetry to dissipate linear momentum away [3–5]. Most of the linear momentum is, however, dissipated away in the last few cycles of the binary evolution leading to a sudden recoil (or kick) on the binary's center of mass near the merger [6–10].

Remnant properties play an important role throughout gravitational wave science. For example, the ringdown spectra of the gravitational radiation are governed by the remnant black hole, which is characterized by the remnant mass, remnant spin, and the kick velocity [11–14]. Access to the remnant properties of the binary is therefore crucial to develop accurate models for the full inspiral-merger-ringdown signal. Accurate estimation of the remnant masses and spins are also necessary to perform null tests of general relativity using gravitational waves [15,16] and probe certain binary formation channels where the remnant black hole may take part in second-generation mergers [17–28].

Properties of the remnant black hole are typically computed either directly from local measurements of the remnant black hole's apparent horizon [29] (possible in a numerical relativity simulation) or through radiated harmonic modes and invoking flux balancing arguments.

*tislam@umassd.edu

These modes can be computed from inspiral-merger-ringdown (IMR) waveform models such as the effective-one-body models [30–35], phenomenological models [36–45], or numerical-relativity surrogates [46–52]. While it is important to follow the fully relativistic nonlinear dynamics of the binary to accurately calculate the remnant properties, this process may be too slow depending on the time taken to generate the necessary data. To overcome this issue, many attempts have been made to develop accurate phenomenological fits to the remnant data by calibrating an analytical ansatz to NR data [3,8,9,53–74]. While this method may be prone to systematic biases due to the choice of the ansatz, special attention is given in exploring large numbers of possible ansatz and quantifying potential overfitting. An alternative approach is to build data-driven surrogate models for the remnant's properties based on NR data [74–76]. While the resulting surrogate models have been shown to be both accurate and fast, these models are only valid in the comparable mass-ratio regime where NR data is plentiful. Extending these remnant models beyond the comparable mass-ratio regime has always been challenging due to the lack of NR simulations, although remarkable progress has been made on this front [72,77–79].

Recently, a numerical-relativity informed point-particle black hole perturbation theory (ppBHPT)-based surrogate model, `BHPTNRSur1dq1e4` [80], was developed for comparable to large mass-ratio binaries [80,81]. The model was validated against a handful of NR waveforms for mass ratios ranging from $q = 15$ to $q = 32$. We will use this model to investigate the remnant properties of high-mass-ratio BBH mergers and to develop accurate remnant fits in this regime. The rest of the paper is organized as follows. In Sec. II, we present an overview of the methods used to compute the properties of the remnant black hole using the `BHPTNRSur1dq1e4` model and provide a prescription to fit the remnant data. We then present our results in Sec. III and discuss a possible implication for waveform modeling in the context of the `BHPTNRSur1dq1e4` model in Sec. IV. Finally, we discuss our results in Sec. V.

II. METHODS

In this section, we first provide an overview of our NR-informed ppBHPT waveform model (Sec. II A). We then present an executive summary of the methods we use to compute the remnant properties of the binary given a gravitational waveform $h(t)$ (Sec. II B). Finally, we summarize the techniques used to build fits for the remnant properties as a function of the binary parameter space (Sec. II C).

A. Overview of the `BHPTNRSur1dq1e4` waveform model

Gravitational radiation from the merger of a binary black hole is typically written as a superposition of -2 spin-weighted spherical harmonic modes with indices (ℓ, m),

$$h(t,\theta,\phi;\boldsymbol{\lambda}) = \sum_{\ell=2}^{\infty}\sum_{m=-\ell}^{\ell} h^{\ell m}(t;\boldsymbol{\lambda})\,{}_{-2}Y_{\ell m}(\theta,\phi), \quad (1)$$

where $\boldsymbol{\lambda}$ is the set of intrinsic parameters (such as the masses and spins of the binary) describing the system, θ is the polar angle, and ϕ is the azimuthal angle.

In this paper, we generate gravitational waveforms primarily using the `BHPTNRSur1dq1e4` model [80]. The model can be accessed through `gwsurrogate` [82,83] or through `BHPTNRSurrogate` [84] package from the `Black Hole Perturbation Theory Toolkit` [85]. This is a surrogate model trained on waveform data generated by the ppBHPT framework for mass ratios varying from $q = 2.5$ to $q = 10^4$. The full IMR ppBHPT waveform training data is computed using a time-domain Teukolsky equation solver, the details of which have appeared in the literature extensively [70,80,81,86–88]. The model includes a total of 50 spherical harmonic modes up to $\ell = 10$, and calibrates these modes to numerical relativity data up to $\ell = 5$ in the comparable mass regime ($2.5 \leq q \leq 10$). In the comparable mass regime, including mass ratios as low as 2.5, the gravitational waveforms generated through ppBHPT were found to agree surprisingly well with those from NR after this simple calibration step with an error of 10^{-3} or less in dominant quadrupolar mode [80,89,90]. When compared to recent Simulating eXtreme Spacetimes and Rochester Institute of Technology NR simulations at mass ratios ranging from $q = 15$ to $q = 128$ the `BHPTNRSur1dq1e4`'s dominant quadrupolar mode agrees well with errors better than $\approx 10^{-3}$ [80,89].

B. Framework to compute the remnant properties

We compute remnant quantities (such as the remnant mass, remnant spin, remnant kick, and peak luminosity) from the gravitational waveform's harmonic modes [71,91–93] mostly following the equations and conventions outlined in Ref. [71], which we provide for completeness. We implement the framework in the `gw_remnant`[1] package and make it publicly available.

1. Remnant mass

The energy flux due to gravitational radiation is given by

$$\dot{E} = \lim_{r\to\infty} \frac{r^2}{16\pi} \sum_{\ell,m} |\dot{h}^{\ell m}|^2, \quad (2)$$

and where we use an overdot to denote ∂/∂_t. Unless otherwise mentioned, we use all available NR-tuned modes up to $\ell = 5$ to compute the energy flux. We also use $G = c = 1$. Integrating the above expression,

[1] https://github.com/tousifislam/gw_remnant [94] with the hash identifier `a11f553949213147ddedac103cbe93141c7d6a15`.

$E(t) = \int_{-\infty}^{t} \dot{E}(t')dt'$, gives the total radiated energy at time t. In many cases, we only have access to $h^{\ell m}$ over a finite duration and wish to know $E(t)$ for a hypothetical, quasicircular BBH system that started from an infinitely large initial orbital separation. Let us define time such that $t = 0$ occurs at the peak of the total waveform amplitude (taken to be $\sum_{\ell m} |h^{\ell m}|$) and let $t_{\rm initial}$ be the start of the waveform modes we have access to. Then the total energy radiated by the hypothetical system at time t can be written as

$$E(t) = E_0 + \int_{t_{\rm initial}}^{t} \dot{E}(t')dt', \tag{3}$$

where the constant E_0 accounts for the energy dissipated in GWs at times $t \leq t_{\rm initial}$. Throughout the paper, we express times in units of the total mass $M = m_1 + m_2$. Let us assume that, at least in early inspiral, the system's binding energy decreases at a rate determined by energy flux due to gravitational radiation, a standard assumption in post-Newtonian (PN) models. We can then estimate E_0 using a PN expression for the binding energy [see Eq. (2.35) of Ref. [95]]

$$\frac{E_{\rm PN}}{M} = -\frac{1}{2}\nu x\left(1 + E_1^{\rm PN} x + E_2^{\rm PN} x^2 + E_3^{\rm PN} x^3\right), \tag{4}$$

with

$$E_1^{\rm PN} = \left(-\frac{3}{4} - \frac{\nu}{12}\right), \tag{5}$$

$$E_2^{\rm PN} = \left(-\frac{27}{8} + \frac{19\nu}{8} - \frac{\nu^2}{24}\right), \tag{6}$$

$$E_3^{\rm PN} = \left(-\frac{675}{64} + \left[\frac{34445}{576} - \frac{205\pi^2}{96}\right]\nu - \frac{155\nu^2}{96} - \frac{35\nu^3}{5184}\right), \tag{7}$$

where $\nu = \frac{q}{(1+q)^2}$ is the symmetric mass ratio, M is the total mass, $x = \omega^{1/3}$, $\omega = \frac{d\phi}{dt}$, and $\phi(t)$ is the orbital phase of the binary. The integration constant,

$$E_0 = -E_{\rm PN}(x(t_{\rm initial})), \tag{8}$$

is then simply given by direct evaluation.

We now consider a model for the remnant mass. Let $M_B(t)$ be the time-dependent Bondi mass of the binary system and $M_{\rm ADM}$ be the Arnowitt-Deser-Misner (ADM) [96] mass. For isolated systems, these two masses are related by [97],

$$M_{\rm ADM} = M_B(t) + \int_{-\infty}^{t} \dot{E}(t')dt'. \tag{9}$$

That is, the ADM mass equals the Bondi mass plus the energy carried away by gravitational radiation. The ADM mass can be directly computed in a numerical relativity simulation but is, of course, unavailable in waveform models. In Appendix, we show that for the nonspinning systems considered here, the ADM mass as computed in a typical NR simulation can be approximated by[2]

$$M_{\rm ADM} \approx M - E_0, \tag{10}$$

where E_0 is the PN binding energy at the start of the waveform. Assuming no gravitational wave emission at times $t \leq t_{\rm initial}$ (which is the case for NR simulations), our modeled Bondi mass is

$$M_B(t) = M - E_0 - \int_{t_{\rm initial}}^{t} \dot{E}(t')dt', \tag{11}$$

from which the remnant mass,

$$\begin{aligned} M_{\rm rem} &= M_B(\infty) \approx M_B(t_{\rm end}) \\ &= M - E_0 - \int_{t_{\rm initial}}^{t_{\rm end}} \dot{E}(t')dt', \end{aligned} \tag{12}$$

is readily computed. Here $t_{\rm end}$ is time at the end of the waveform, set to be $t_{\rm end} \approx 115M$ in the `BHPTNRSur1dq1e4` model. Our remnant model and the assumptions underlying it are supported by Fig. 1 (top row), where we compare to the remnant mass computed directly from the final black hole's apparent horizon (solid red line).

2. Remnant-kick velocity

The time derivative of the radiated linear momenta is expressed as [71]

$$\begin{aligned} \frac{dP_x}{dt} = \lim_{r\to\infty} \frac{r^2}{8\pi} \Re\Bigg[\sum_{\ell,m} \dot{h}^{\ell m}\Big(a_{\ell m}\dot{\bar{h}}^{\ell,m+1} \\ + b_{\ell,-m}\dot{\bar{h}}^{\ell-1,m+1} - b_{\ell+1,m+1}\dot{\bar{h}}^{\ell+1,m+1}\Big)\Bigg], \end{aligned} \tag{13}$$

$$\begin{aligned} \frac{dP_y}{dt} = \lim_{r\to\infty} \frac{r^2}{8\pi} \Im\Bigg[\sum_{\ell,m} \dot{h}^{\ell m}\Big(a_{\ell m}\dot{\bar{h}}^{\ell,m+1} \\ + b_{\ell,-m}\dot{\bar{h}}^{\ell-1,m+1} - b_{\ell+1,m+1}\dot{\bar{h}}^{\ell+1,m+1}\Big)\Bigg], \end{aligned} \tag{14}$$

[2]This dependency can be understood by noting that there is no gravitational radiation content at the start of an NR simulation. Consequently, the ADM mass as computed in NR will depend only on the initial data (such as the initial coordinate separation of the two black holes) prescribed on the finite computational domain. For example, see Table 1 of Ref. [98].

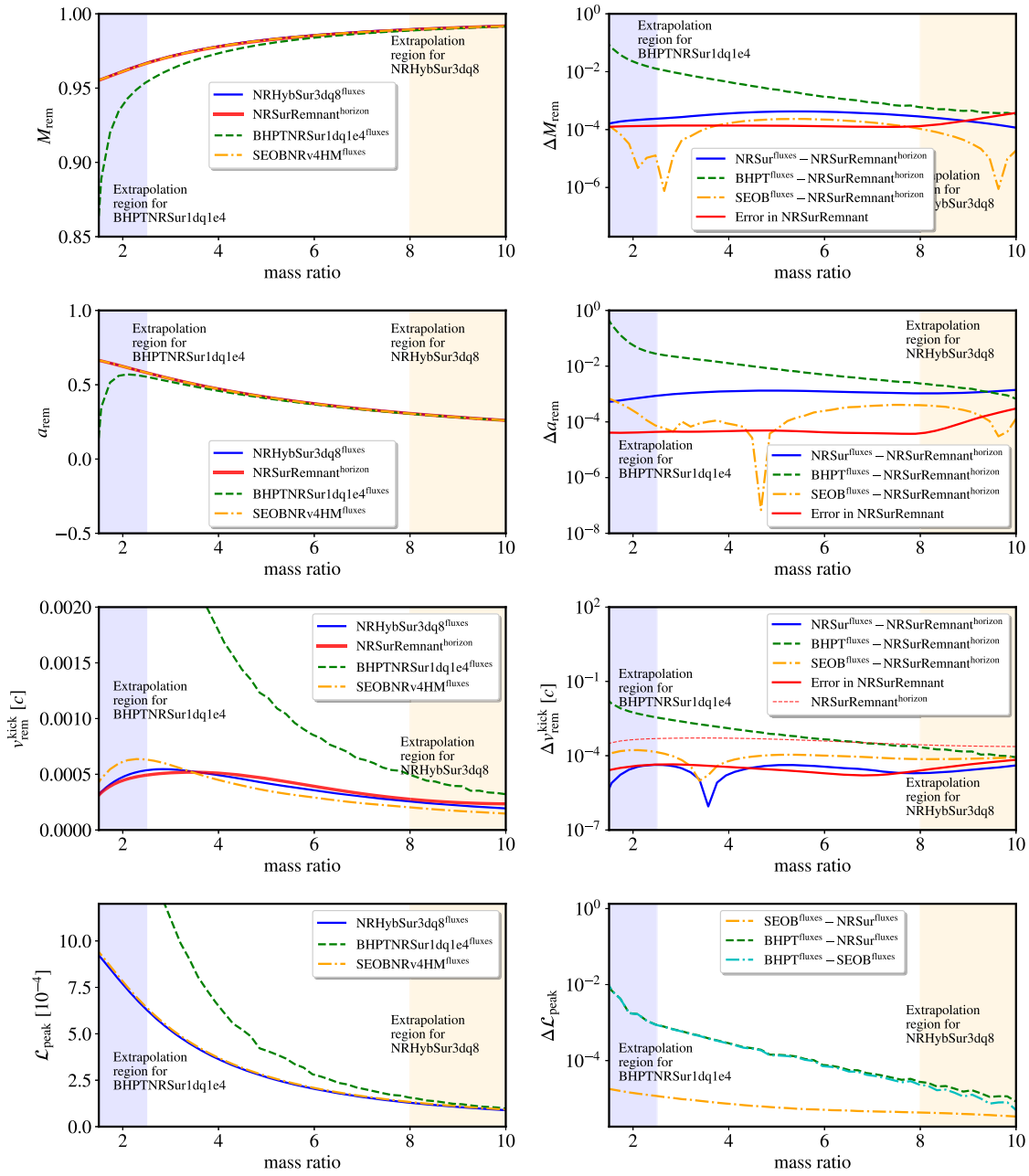

FIG. 1. Remnant quantities computed from three different waveform models `BHPTNRSur1dq1e4` (dashed green), `SEOBNRv4HM` (dash-dot yellow), and `NRHybSur3dq8` (solid blue), as well as from `NRSur3dq8Remnant` (solid red). The mass and spin values are computed either directly from apparent horizon measurements (`NRSur3dq8Remnant`) or gravitational wave fluxes (`BHPTNRSur1dq1e4`, `SEOBNRv4HM`, `NRHybSur3dq8`). We show remnant mass $M_{\rm rem}$, remnant spin $a_{\rm rem}$, remnant-kick velocity $v^{\rm kick}_{\rm rem}$ and the peak luminosity $\mathcal{L}_{\rm peak}$ in the left column and respective differences with `NRSur3dq8Remnant` or other waveform models in the right column. We further show the GRP fit uncertainties in the `NRSur3dq8Remnant` estimates. Shaded regions indicate the respective regions where `BHPTNRSur1dq1e4` (blue) and `NRHybSur3dq8` (yellow) models are extrapolated outside their training region, respectively. Details can be found in the text. To put kick-velocity errors into perspective, we also show the `NRSur3dq8-Remnant` predictions as a dashed red line.

$$\frac{dP_z}{dt} = \lim_{r\to\infty}\frac{r^2}{16\pi}\sum_{\ell,m}\dot{h}^{\ell m}\Big(c_{\ell m}\dot{\bar{h}}^{\ell m} + d_{\ell m}\dot{\bar{h}}^{\ell-1,m} + d_{\ell+1,m}\dot{\bar{h}}^{\ell+1,m}\Big), \tag{15}$$

where the upper bar denotes complex conjugation and the coefficients $a_{\ell,m}$, $b_{\ell,m}$, $c_{\ell,m}$, and $d_{\ell,m}$ are given in Ref. [71]. Integrating $d\mathbf{P}/dt$ then gives us the radiated linear momentum of the binary as a function of time. While integrating, we set the integration constant to be zero as the linear

momentum emission at early inspiral is expected to be negligible when averaged over an orbital cycle. The time-dependent kick imparted to the system's center of mass is then,

$$\mathbf{v}(t) = -\frac{P_x(t)\hat{\mathbf{x}} + P_y(t)\hat{\mathbf{y}} + P_z(t)\hat{\mathbf{z}}}{M_B(t)}, \tag{16}$$

and taking the magnitude

$$v_{\rm rem}^{\rm kick} = |\mathbf{v}(t = t_{\rm end})|, \tag{17}$$

gives the kick velocity of the remnant.

3. Remnant spin

The rate of loss of angular momentum during binary evolution has the following form [71]:

$$\frac{dJ_x}{dt} = \lim_{r\to\infty}\frac{r^2}{32\pi}\Im\left[\sum_{\ell m} h^{\ell m}\left(f_{\ell m}\dot{\bar{h}}^{\ell,m+1} + f_{\ell,-m}\dot{\bar{h}}^{\ell,m-1}\right)\right], \tag{18}$$

$$\frac{dJ_y}{dt} = -\lim_{r\to\infty}\frac{r^2}{32\pi}\Re\left[\sum_{\ell,m} h^{\ell m}\left(f_{\ell m}\dot{\bar{h}}^{\ell,m+1} - f_{\ell,-m}\dot{\bar{h}}^{\ell,m-1}\right)\right], \tag{19}$$

$$\frac{dJ_z}{dt} = \lim_{r\to\infty}\frac{r^2}{16\pi}\Im\left[\sum_{\ell,m} m h^{\ell m}\dot{\bar{h}}^{\ell m}\right], \tag{20}$$

where

$$f_{\ell m} = \sqrt{\ell(\ell+1) - m(m+1)}. \tag{21}$$

To compute the total loss of the angular momentum since the start of the waveform, we integrate $d\mathbf{J}/dt$.

For the nonspinning BBH systems considered here, the orbital motion is confined to the x-y plane. Let J_z^0 be the orbital angular momentum at the start of the waveform, then invoking a flux balancing argument, we can estimate the remnant spin of the final black hole by [99]

$$a_{\rm rem} = \frac{J_z^0 - J_z^{\rm rad}}{M_{\rm rem}^2}, \tag{22}$$

where $J_z^{\rm rad}$ is the total loss of angular momentum since the start of the waveform and, due to the symmetry of the systems we consider, the final spin is always in the z direction. We estimate J_z^0 using a post-Newtonian expression for the angular momentum [see Eq. (2.36) of Ref. [95]]

$$\frac{J_{\rm PN}}{M^2} = \frac{\nu}{x^{1/2}}(1 + J_1^{\rm PN}x + J_2^{\rm PN}x^2 + J_3^{\rm PN}x^3), \tag{23}$$

where

$$J_1^{\rm PN} = \left(\frac{3}{2} + \frac{\nu}{6}\right), \tag{24}$$

$$J_2^{\rm PN} = \left(\frac{27}{8} - \frac{19\nu}{8} + \frac{\nu^2}{24}\right), \tag{25}$$

$$J_3^{\rm PN} = \left(\frac{135}{16} + \left[-\frac{6889}{144} + \frac{41\pi^2}{24}\right]\nu + \frac{31\nu^2}{24} + \frac{7\nu^3}{1296}\right). \tag{26}$$

The integration constant J_z^0 is then taken to be $J_{\rm PN}(x(t_{\rm initial}))$.

4. Peak luminosity

We calculate the peak value luminosity,

$$\mathcal{L}_{\rm peak} = \max_t \dot{E}, \tag{27}$$

by fitting a quadratic function to 21 adjacent samples of $\dot{E}$, consisting of the largest sample and ten neighbors on either side. The peak luminosity can then be found analytically from the fit. Here, we use the same set of modes that are used to compute other remnant quantities.[3]

C. Building fits for the remnant properties

One of the primary objectives of this paper is to provide accurate fits to the remnant properties for both comparable and large mass ratio BBH mergers. We first compute the remnant properties—remnant mass $M_{\rm rem}$, remnant spin $a_{\rm rem}$, remnant kick velocity $v_{\rm rem}^{\rm kick}$, and the peak luminosity $\mathcal{L}_{\rm peak}$—using gravitational waveforms generated with the `BHPTNRSur1dq1e4` model.

For the remnant mass, we choose to fit $\log_{10}(1 - M_{\rm rem})$ instead of $M_{\rm rem}$ as it has a better-behaved functional form over a large range of mass ratios leading to more accurate fits. For the same reason, we build fits for $\log_{10}(a_{\rm rem})$, $\log_{10}(v_{\rm rem}^{\rm kick})$, and $\log_{10}(\mathcal{L}_{\rm peak})$. All of our fits are parametrized by $\log_{10}(q)$. To construct the fits, we use the Gaussian process regression (GPR) [100] methods as implemented in `scikit-learn` [101] with radial basis functions kernels. When the models are evaluated, we can easily get the predicted remnant by undoing these transformations.

[3]Since we use $G = c = 1$ in the paper, no units are used for luminosity.

III. RESULTS

In this section, we first present a comparison between remnant properties computed using the BHPTNRSur1dq1e4 model and other state-of-art waveform models in the comparable mass ratio regime (Sec. III A) and compare with RIT NR data in the intermediate mass ratio regime (Sec. III B). Finally, we build GPR fits for the remnant quantities, obtained using BHPTNRSur1dq1e4, for all mass ratios (Sec. III C).

A. Comparison against NR surrogates in the comparable mass-ratio regime

We first compute remnant quantities in the comparable mass ratio regime ($1 \leq q \leq 10$) using three different waveform models: BHPTNRSur1dq1e4, NRHybSur3dq8 [49] and SEOBNRv4HM [102]. NRHybSur3dq8 is a surrogate model for hybridized NR waveforms from aligned-spin BBH mergers trained on 104 NR waveforms for mass ratio $1 \leq q \leq 8$ and spin $|\chi_1, \chi_2| \leq 0.8$. The model can, however, be extrapolated up to mass ratio $q \approx 10$. The model includes all spin-weighted spherical harmonic modes up to $\ell = 4$ and the $(5, \pm 5)$ but not the $(4, \pm 1)$ or (4,0) modes. SEOBNRv4HM is a state-of-art effective-one-body model for the aligned-spin binaries and has the following four higher-order modes apart for the dominant quadrupolar mode of radiation: $\{(\ell, m) = \{(2, \pm 1), (3, \pm 3), (4, \pm 4), (5, \pm 5)\}$. We use both NRHybSur3dq8 and SEOBNRv4HM in their nonspinning limit. For all models, we generate waveforms on the same time grid $t \in [-5000, 100]M$ with time spacing $dt = 0.1M$. To compute the remnant quantities, we use the following set of modes for both BHPTNRSur1dq1e4 and NRHybSur3dq8 models: $\{(\ell, m) = \{(2, \pm 2), (2, \pm 1), (3, \pm 1), (3, \pm 2), (3, \pm 3), (4, \pm 2), (4, \pm 3), (4, \pm 4)\}$.[4] For SEOBNRv4HM, we use all available modes.

In Fig. 1, we show the remnant mass, remnant spin, remnant-kick velocity, and the peak luminosity $\mathcal{L}_{\rm peak}$ estimated from these three different waveform models (left column). For comparison, we also show remnant quantities computed from the NRSur3dq8Remnant model [75]. Notably, NRSur3dq8Remnant predicts the remnant mass and spin values determined *directly* from the final black hole's apparent horizon [29], whereas we use fluxes computed from waveform modes where the integration constants are set from PN. A careful comparison of remnant properties from horizon data and asymptotic data in numerical relativity simulations was recently reported on by Iozzo *et al.* [103].

We find that the remnant quantities obtained from waveforms generated with NRHybSur3dq8 model match closely to the values obtained from the NRSur3dq8Remnant model, indicating the effectiveness of the assumptions underlying the framework to compute remnant quantities entirely from gravitational wave data (cf. Sec. II B). It is not surprising that the remnant estimates from the BHPTNRSur1dq1e4 waveforms (which are computed within perturbation theory) differ from the NRSur3dq8Remnant estimates in the comparable mass regime. These differences quickly reduce as we increase the mass ratio. For instance, when $q \geq 8$, remnant mass and spin estimates from the BHPTNRSur1dq1e4 model exhibit excellent match with the ones obtained from other waveform models (NRHybSur3dq8 and SEOBNRv4HM) used in this work. For the kick velocities, even though some visually noticeable differences still remain, they seem to be small. We further note that while remnant mass and spin estimates obtained from SEOBNRv4HM match NRSur3dq8Remnant quite well, visible differences between them exists for the kick velocity estimates. While we cannot make extensive comparisons to NR for $q \geq 10$, the BHPTNRSur1dq1e4 model (and hence remnant quantities computed from it) is expected to become more accurate in the high-mass-ratio regime where perturbation theory is more applicable.

B. Validation against RIT NR data in the intermediate mass-ratio regime

To further check the remnant properties estimated from the BHPTNRSur1dq1e4 model, we validate our results against a handful of recently available NR simulations in the intermediate mass ratio range at $q = [15, 32, 64]$ [78]. Figure 2 shows the kick velocity profile $v_{\rm kick}(t)$, the radiated angular momentum profile $J(t)$, and the radiated energy profile $E(t)$ computed with waveforms generated from the BHPTNRSur1dq1e4 model using the following set of modes: $\{(\ell, m) = \{(2, \pm 2), (2, \pm 1), (3, \pm 1), (3, \pm 2), (3, \pm 3), (4, \pm 2), (4, \pm 3), (4, \pm 4)\}$. We validate these results against the respective profiles estimated from the RIT NR data using the same set of modes. For further comparison, we also include remnant profiles estimated from the SEOBNRv4HM waveforms using all modes available for that model. We note that the NR waveforms only provide the last $\sim 2000M$ of the binary's evolution, so we use the same length of waveform data from BHPTNRSur1dq1e4 and SEOBNRv4HM models. We find that the remnant profiles obtained from the BHPTNRSur1dq1e4 model are consistent with the NR data. While some small discrepancies are apparent in the figure, we note that the high-mass-ratio NR waveforms appear to have some residual eccentricity [35] that could account for this.

C. Fits for remnant properties for all mass ratios

Results obtained in Secs. III A and III B demonstrate that the BHPTNRSur1dq1e4 waveform model can be used to predict the remnant properties in the intermediate mass ratio regime. Next, we build fits for the remnant mass,

[4] We only use modes up to $\ell \leq 4$ that are available in BHPTNRSur1dq1e4 model.

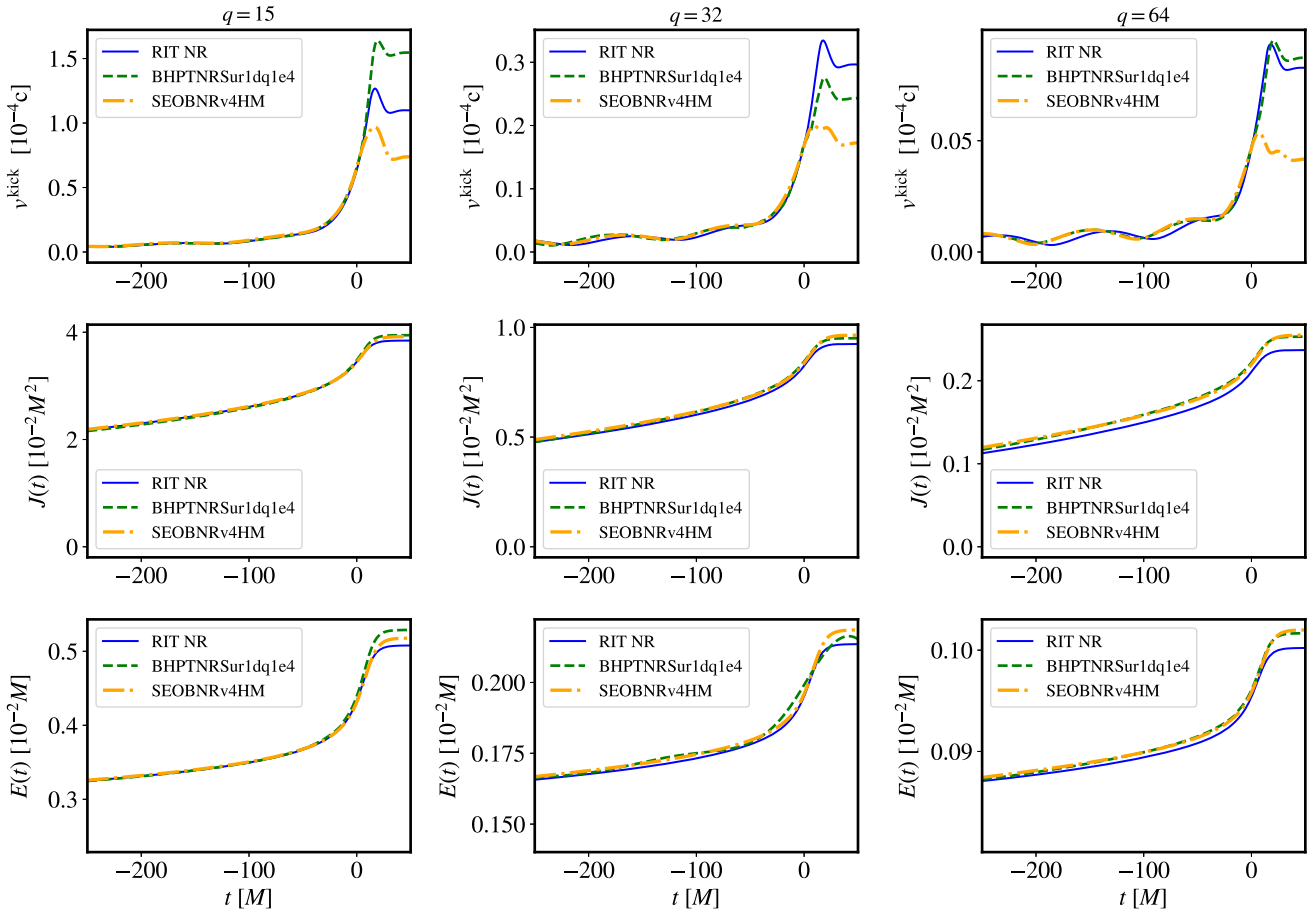

FIG. 2. We show the kick velocity profile $v_{\rm kick}$, the time-dependent radiated angular momentum profile $J(t)$ and the radiated energy profile $E(t)$ for three different mass ratio values: $q = 15$ (left column), $q = 32$ (middle column) and $q = 64$ (right column). We show the profiles obtained from the RIT NR data (solid blue lines), the `BHPTNRSur1dq1e4` model (green dashed lines), and the `SEOBNRv4HM` model (orange dash-dotted lines).

remnant spin, remnant-kick velocity, and peak luminosity as a function of the mass ratio in the range $q \in [2, 1000]$. We first choose 200 different values of q distributed uniformly in $\log_{10}(q)$. Following the framework described in Sec. II B and using the `BHPTNRSur1dq1e4` model, we compute the remnant properties at these mass ratios. These remnant values will serve as both training and validation datasets.

1. GPR fits

We divide the remnant dataset randomly into two separate groups using 100 data points for training and 100 data points for validation. Model fitting is performed using the procedure described in Sec. II C.

In Fig. 3 (*left column*), we show both the training data as well as the GPR prediction (given by the GPR model's mean values) as a function of the parameter space. The right column compares the fit outputs against the validation data set and the estimated GPR fit uncertainties. Based on the accuracy, we find that our fits are most useful at $q \geq 10$, which is sufficient for our purpose as other models (e.g., `NRSur3dq8Remnant`) have been developed for mass ratios $q \leq 10$. Our model complements these by working in the large mass-ratio regime. We make our remnant fits publicly available through the `BHPTNR_Remnant`[5] package [104].

2. Analytical fit for the kick velocity

As a final piece in our fitting exercise, we revisit the analytical kick velocity fits obtained by Sundararajan, Khanna, and Hughes (hereafter `SKH`) [70]. They had modeled the kick-velocity profile's peak,

$$v_{\rm kick}^{\rm peak} = 0.051 \times (1/q)^2, \tag{28}$$

and late-time (final) kick,

$$v_{\rm kick}^{\rm late} = 0.044 \times (1/q)^2. \tag{29}$$

[5] https://github.com/tousifislam/BHPTNR_Remnant with the hash identifier `ca79e050a81c0f0d1ce5aad71b52b108c42e2c6f`.

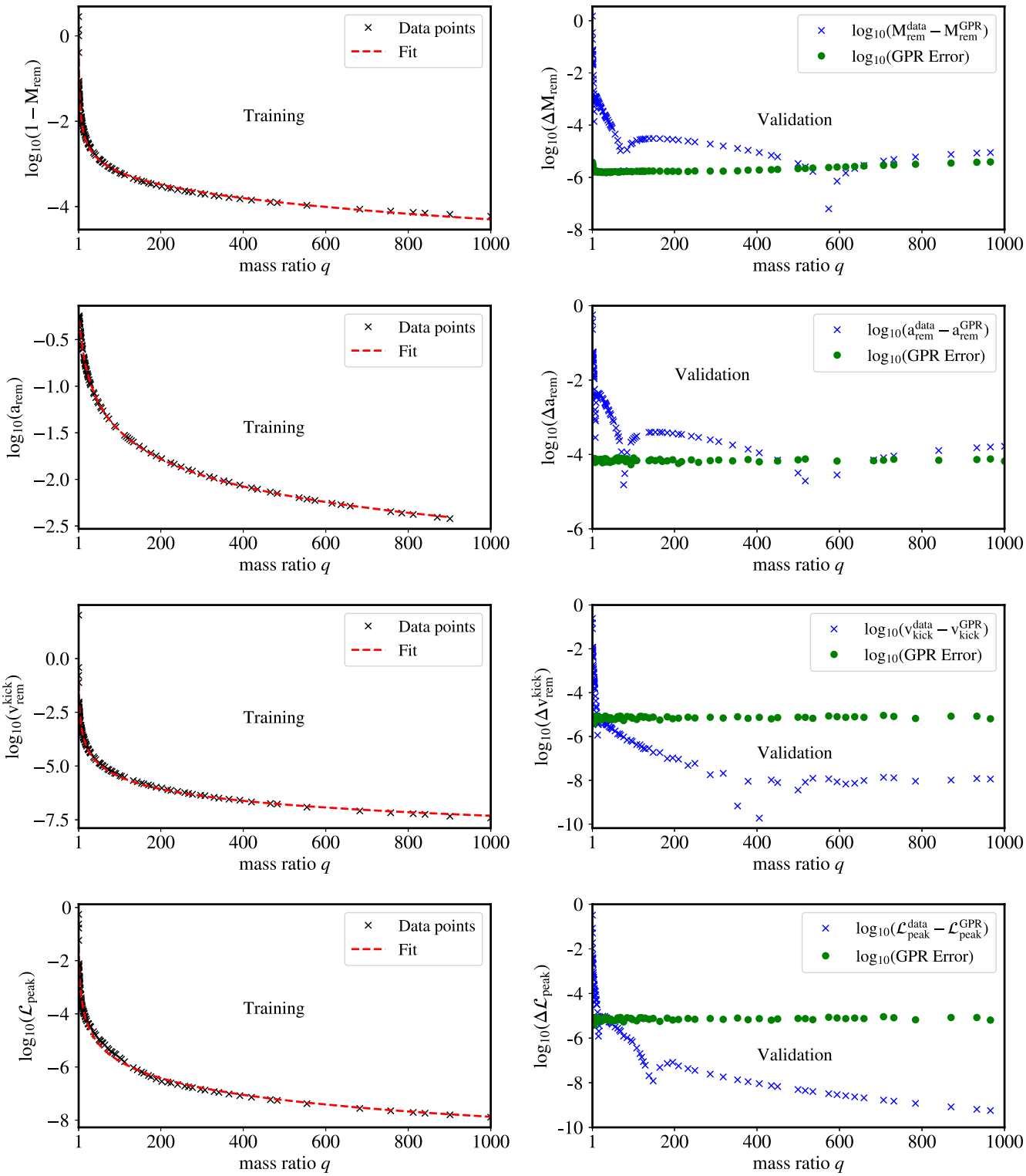

FIG. 3. *Left column:* We show the training data (black crosses) and the GPR model's prediction (red dashed line) as a function of the mass ratio for $M_{\rm rem}$, $a_{\rm rem}$, $v^{\rm kick}_{\rm rem}$ and $\mathcal{L}_{\rm peak}$. *Right panel:* we show the underlying GPR-fit uncertainties (green circles) and the difference between the data and mean GPR predictions (blue crosses) in our validation set. Please note that the fit uncertainties ("GPR Error") are for the fitted data [e.g., $\log_{10}(1 - M_{\rm rem})$] while the fit errors are for the remnant quantities (e.g., $M^{\rm data}_{\rm rem} - M^{\rm GPR}_{\rm rem}$).

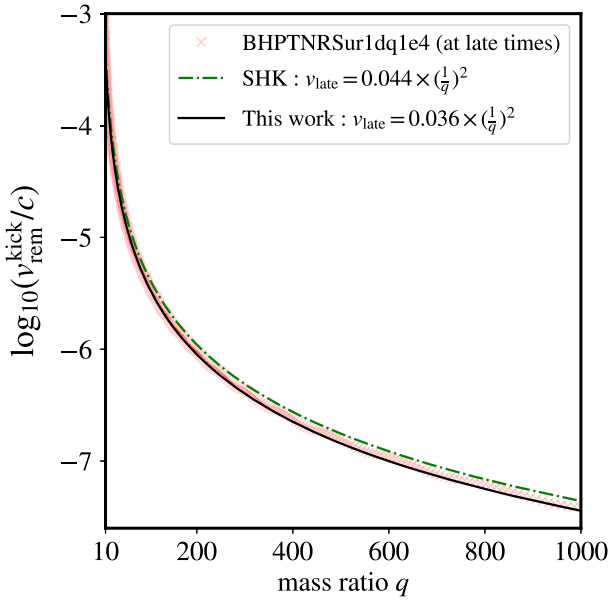

FIG. 4. We show the kick velocities $v^{\rm kick}_{\rm rem}$ (at late times) estimated from the BHPTNRSur1dq1e4 model (at late times) as a function of mass ratio q (red crosses) along with the predictions from the fitted kick velocity formula from SKH [70] (green dash-dotted line). We also show the updated analytical fit in black.

In Fig. 4, we show the remnant kick magnitudes (at late times) estimated from the BHPTNRSur1dq1e4 model as a function of the mass ratio q along with the late-time kick velocities obtained from SKH fits. We find that SKH fits result in a larger magnitude of kicks throughout the mass-ratio range considered in this work. This is not surprising as the NR-informed BHPTNRSur1dq1e4 model yields a smaller amplitude than the raw ppBHPT waveforms used in obtaining SKH fits. While there could be additional explanations for discrepancies, the known differences in amplitude are likely to be one of the main reasons why the kick velocities obtained from the BHPTNRSur1dq1e4 model are systematically smaller than the values obtained from SKH fits. However, the functional form used in SKH fits catches the key behavior of the kick velocity. This suggests that one can possibly improve the SKH kick velocity model by updating the fit coefficients. Using `scipy.optimize.curve_fit` [105], we obtain the following fitted formula for the kick velocity:

$$v^{\rm late}_{\rm kick} = (0.03433 \pm 0.00003) \times (1/q)^2. \quad (30)$$

We find that the updated kick-velocity fit matches the estimated kicks from the BHPTNRSur1dq1e4 model quite well for mass ratio $q \geq 5$. The fit accuracy further improves when we fit the data for $q \geq 10$. In that case, we find the late-time and peak kick formula to be

$$v^{\rm late}_{\rm kick} = (0.03694 \pm 0.00008) \times (1/q)^2, \quad (31)$$

$$v^{\rm peak}_{\rm kick} = (0.0401 \pm 0.0002) \times (1/q)^2. \quad (32)$$

It has been previously argued in Ref. [106] that one can improve the ability of ppBHPT to extrapolate out of the perturbative regime by replacing the q^{-2} factor, which describes the momentum flux and the recoil velocity with $f(q) = \frac{1}{q^2}\sqrt{1-\frac{4}{q}}$. We verify that applying the $\frac{1}{q^2} \to f(q)$ rule on Eqs. (28) and (29) only changes the fit behavior in the small mass-ratio regime (for $q \leq 20$) while for larger mass ratios both fits give similar results.

D. Comparison between BHPTNR_Remnant and phenomenological models in the intermediate mass-ratio regime

At this point, we compare the predictions of the BHPTNR_Remnant model for the final mass and spin with a widely used phenomenological fit referred to as the "UIB fits" [74]. The UIB fits are constructed using NR data in the comparable mass regime and analytical results in the test-particle limit. We specifically examine their outputs in the different mass-ratio regimes; $3 \leq q \leq 1000$. Figure 5 shows the relative differences in the remnant mass

$$\Delta M_{\rm rem} = \frac{M^{\rm BHPTNR}_{\rm rem} - M^{\rm UIB}_{\rm rem}}{M^{\rm BHPTNR}_{\rm rem}}$$

and in remnant spin

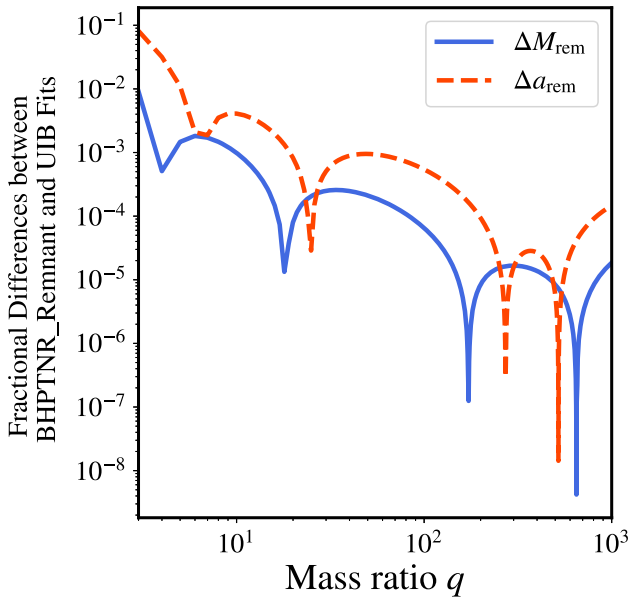

FIG. 5. We show the relative differences in remnant mass (solid blue line) and remnant spin (dashed red line) estimates between BHPTNR_Remnant model and phenomenological models (referred to as 'UIB') presented in Ref. [74] as a function of mass ratio.

$$\Delta a_{\rm rem} = \frac{a_{\rm rem}^{\rm BHPTNR} - a_{\rm rem}^{\rm UIB}}{a_{\rm rem}^{\rm BHPTNR}}$$

between these two models as a function of mass ratio. We observe that as the mass ratio increases, the differences between the models decrease. However, in the intermediate mass-ratio regime ($10 \leq q \leq 100$), the typical differences between these two models are on the order of $\sim 10^{-4}$ for the remnant mass and $\sim 10^{-3}$ for the remnant spin.

IV. APPLICATION TO WAVEFORM MODELING

We now explore whether the estimated remnant properties may help ongoing efforts to build waveform models based on the ppBHPT framework. For simplicity, we restrict ourselves to the (2,2) mode. To better appreciate the problem, consider Fig. 8 of Ref. [80], where we see noticeable disagreements between the peak amplitude of a $q = 4$ waveform computed with `BHPTNRSur1dq1e4` (solid red) and `NRHybSur3dq8` (black dashed). One explanation for this disagreement could be that within the ppBHPT framework, the remnant's value is equal to the mass of the primary, which is not physically correct. We would like to understand whether access to the remnant black hole's properties will help improve the `BHPTNRSur1dq1e4`'s merger and ringdown signal at comparable to intermediate-mass ratios.

We first recall that while the `BHPTNRSur1dq1e4` model is based on perturbation theory, the waveforms are calibrated to NR according to the formula,

$$h^{22}_{\texttt{BHPTNRSur1dq1e4},\alpha,\beta}(t;q) = \alpha h^{22}_{\texttt{ppBHPT}}(t\beta;q), \quad (33)$$

where the dominant quadrupole, $h^{22}_{\texttt{ppBHPT}}$, is computed using a high-order Teukolsky equation solver. Optimal values of α and β are obtained by minimizing the difference

$$\min_{\alpha,\beta} \int \left| h^{22}_{\texttt{BHPTNRSur1dq1e4},\alpha,\beta}(t;q) - h^{22}_{\rm NRHyb}(t;q) \right|^2 dt, \quad (34)$$

between our model `BHPTNRSur1dq1e4` and a hybridized NR surrogate waveform `NRHybSur3dq8` [49] in its nonspinning limit over the time window $t \in [-5000, 115]$ M. Because the calibration is performed using the full IMR waveform having almost $\sim$5000 M of the inspiral data and only $\sim$100 M of the merger ringdown data, our α-β calibration procedure is heavily influenced by the inspiral portion of the waveform. The merger-ringdown portion of the signal will, of course, be controlled by the remnant properties, which has not been taken into account separately. For example, we expect the binary to shed mass and angular momentum as it advances towards merger, which will change the waveform's postmerger signal by decreasing the amplitude. One simple approach within our modelization setup is to allow the value of α and β to vary between the inspiral and merger-ringdown part of the waveform. While this method will result in better matches to NR data in both the inspiral and the merger-ringdown part, it will also increase the number of free parameters by a factor of two.

Let us consider physically motivated scaling factors $\{\xi_\alpha, \xi_\beta\}$ that will rescale the already calibrated ppBHPT waveform in the postmerger signal according to

$$\alpha_{\rm MR} = \xi_\alpha \times \alpha_{\rm IMR}, \qquad \beta_{\rm MR} = \frac{\beta_{\rm IMR}}{\xi_\beta}, \quad (35)$$

where $\alpha_{\rm IMR}$ and $\beta_{\rm IMR}$ are the original calibration parameters used to build the `BHPTNRSur1dq1e4` model (and are mostly influenced by the inspiral part of the waveform) and $\alpha_{\rm MR}$ and $\beta_{\rm MR}$ are new calibration parameters for the merger-ringdown waveform. This approach will keep the number of free parameters in our model unchanged if $\{\xi_\alpha, \xi_\beta\}$ can be determined without any extra free parameters. An obvious choice is to assume they are functions of the remnant mass and spin or, in a similar spirit, the radiated energy and angular momentum.

By solving the relevant optimization problem, we first compute optimal values of $\alpha^{\rm opt}_{\rm MR}$ and $\beta^{\rm opt}_{\rm MR}$ for a set of different mass ratios in the comparable mass regime, $2 \leq q \leq 10$, and plot their behavior in Fig. 6. For comparison, we also plot $\alpha_{\rm IMR}$ and $\beta_{\rm IMR}$ as well as the scaling factor $\alpha = \beta = (1 + 1/q)^{-1}$ that, if used in Eq. (33), would account for the mass scale difference between ppBHPT (the mass scale is taken to be the primary m_1) and NR (the mass scale is taken to be the total mass $m_1 + m_2$ for nonspinning systems); see Refs. [80,81] for further discussion.

We now experiment with different functional forms for $\{\xi_\alpha, \xi_\beta\}$. We first compute the optimal factors, $\xi^{\rm opt}_\alpha$ and $\xi^{\rm opt}_\beta$, from $\alpha^{\rm opt}_{\rm MR}$, $\beta^{\rm opt}_{\rm MR}$, $\alpha_{\rm IMR}$, and $\beta_{\rm IMR}$. In Fig. 7, we show $\xi^{\rm opt}_\alpha$ and $\xi^{\rm opt}_\beta$ as a function of the mass ratio. We find that the values for $\xi^{\rm opt}_\alpha$ and $\xi^{\rm opt}_\beta$ are quite close to each other. For simplicity of demonstration, we fix $\xi_\alpha = \xi_\beta = \xi$ and consider three possible choices for the scaling factor:

(i) $\xi = (1 - \frac{\Delta E}{M})$,
(ii) $\xi = (1 - \frac{\Delta J^z}{M^2})(1 - \frac{\Delta E}{M})$,
(iii) $\xi = [1 - (\frac{\Delta J^z}{M^2})^{1.5}](1 - \frac{\Delta E}{M})$,

where ΔE and ΔJ^z are the total radiated energy and total radiated angular momentum until $t_{\rm ref} = -100$ M. The choice of $t_{\rm ref} = -100$ M is motivated by the intuition that the mass and the spin of the binary at the end of the plunge should characterize the merger-ringdown signal. We explored different choices of $t_{\rm ref}$ and found $t_{\rm ref} = -100$ M to consistently provide a better agreement between the postmerger signals. In other words, $\alpha_{\rm MR}$ and $\beta_{\rm MR}$ should be related to the total loss of energy and angular momentum at plunge. Figure 7 shows the behavior of each choice of ξ.

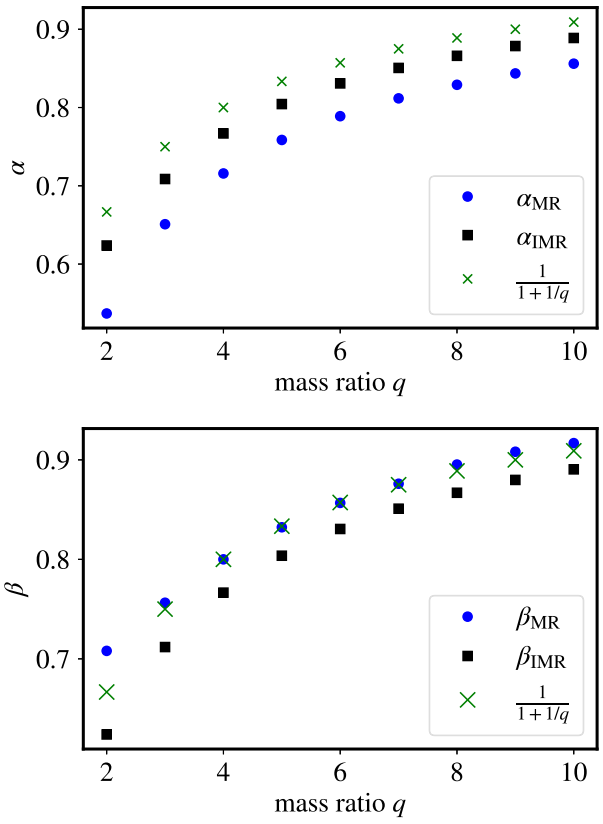

FIG. 6. We show the α (upper panel) and β (upper panel) values used in the `BHPTNRSur1dq1e4` model (denoted by $\alpha_{\rm IMR}$ and $\beta_{\rm IMR}$ respectively) as well as the ones computed using only the merger-ringdown part of the waveforms (denoted by $\alpha_{\rm MR}$ and $\beta_{\rm MR}$ respectively). For comparison, we also show the simple scaling factor $\frac{1}{1+1/q}$ needed to account for different definitions of the mass scale in NR and ppBHPT.

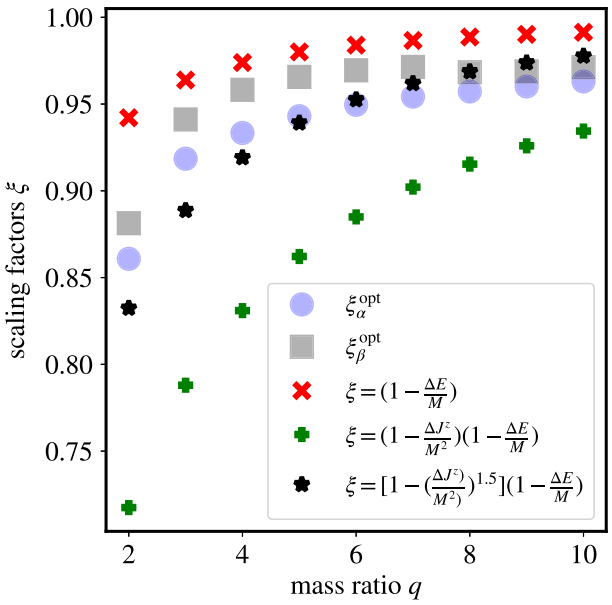

FIG. 7. We show the optimal scaling factors $\xi_\alpha^{\rm opt}$ (blue circles) and $\xi_\beta^{\rm opt}$ (gray squares) needed to take the $\alpha_{\rm IMR}$ and $\beta_{\rm IMR}$ (scaling factors stemming from inspiral-merger-ringdown waveform data) to $\alpha_{\rm MR}^{\rm opt}$ and $\beta_{\rm MR}^{\rm opt}$ (scaling factors stemming from merger-ringdown waveform data only), respectively [see Fig. 6 and Eq. (35)]. We also show three different proposed functional forms of ξ for comparison.

We now demonstrate a possible way of incorporating the remnant information into the `BHPTNRSur1dq1e4` model. In Fig. 8, we show the amplitude of the dominant (2,2) mode of a $q=8$ waveform in the merger-ringdown part. We see a noticeable difference between the `BHPTNRSur1dq1e4` model and `NRHybSur3dq8` model. In particular, `BHPTNRSur1dq1e4` predicts a larger amplitude. We employ the following procedure to incorporate the remnant information into the model. We first evaluate the `BHPTNRSur1dq1e4` harmonic modes, from which the remnant properties can be computed. We then rescale the postmerger waveform using the scaling factor $\xi=(1-\frac{\Delta J^z}{M^2})(1-\frac{\Delta E}{M})$. Finally, we hybridize the inspiral and postmerger parts using a smooth partition of unity [107],

$$h_{\rm hybrid}(t) = (1-\Phi(t)) \times h_{\rm ins}(t;\alpha_{\rm IMR},\beta_{\rm IMR}) + \Phi(t) \times h_{\rm MR}(t;\alpha_{\rm MR},\beta_{\rm MR}), \quad (36)$$

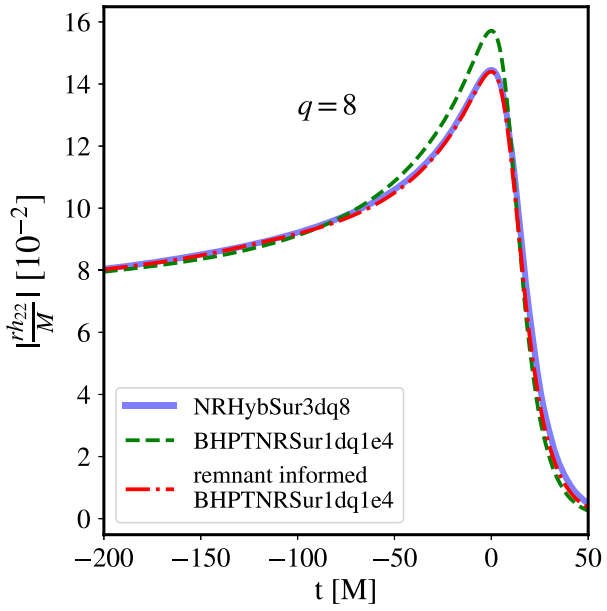

FIG. 8. We demonstrate how the remnant properties would help build better waveform models for the merger ringdown part of the waveform. We show the amplitude of the `BHPTNRSur1dq1e4` waveform and the `NRHybSur3dq8` waveform for $q=8$. For comparison, we then show the remnant informed `BHPTNRSur1dq1e4` waveform too.

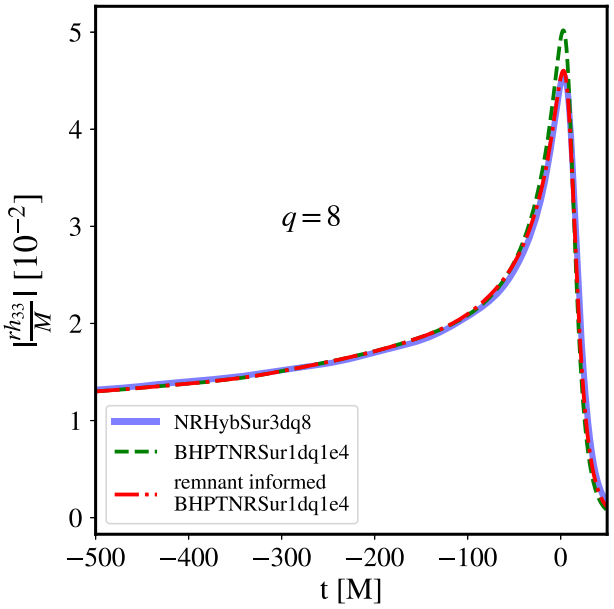

FIG. 9. We demonstrate how the remnant properties would help build better waveform models for the merger ringdown part of the waveform for the (3,3) mode. We show the amplitude of the BHPTNRSur1dq1e4 waveform and the NRHybSur3dq8 waveform for $q = 8$. For comparison, we then show the remnant informed BHPTNRSur1dq1e4 waveform too.

where $\Phi(t)$ is an appropriate bump function (e.g., Planck window function).

We find that the remnant-informed BHPTNRSur1dq1e4 model matches the NR data much better than the usual BHPTNRSur1dq1e4 model. While the overall L_2-norm error, computed over the full IMR signal, only improves from 5.8×10^{-4} to 4.6×10^{-4}, the improvement in the merger-ringdown part is much larger as clearly seen from Fig. 8. We also find that the prescription works reasonably well for the higher modes too. As an example, we show the (3,3) mode for $q = 8$ in Fig. 9. While this simple example demonstrates the possible benefits of a remnant-informed BHPTNRSur1dq1e4, achieving highly accurate postmerger matches across all harmonic modes will be taken up in future work.

V. DISCUSSION AND CONCLUSION

The merger of two black holes results in a boosted Kerr black hole that is often referred to as the remnant. In this paper, we implement a framework to compute the final mass, final spin, and kick of the remnant black hole using gravitational waveform modes (to compute fluxes) and post-Newtonian formula to set the relevant integration constants. We make this framework publicly available through the gw_remnant Python package.

Using the gw_remnant package, we compute remnant quantities from the waveforms generated with the BHPTNRSur1dq1e4 model, comparing with the NRHybSur3dq8 and SEOBNRv4HM models as well as RIT NR waveform data at $q = [15, 32, 64]$. We find that remnant quantities found from the BHPTNRSur1dq1e4 model match these other models at mass ratios $q \geq 8$, which is to be expected as BHPTNRSur1dq1e4 is based on black hole perturbation theory and, therefore, is most applicable for intermediate- to large-mass ratio systems. We also compare flux-based remnant quantities to the ones found from the NRSur3dq8Remnant model that relies on quasilocal measurements on the remnant's apparent horizon to compute the final mass, spin, and kick. This provides a nontrivial comparison between remnant properties from waveform data and apparent horizon measurements performed in NR simulations.

We also build surrogate models for the remnant properties of nonspinning BBH mergers as a function of mass ratios ranging from $q = 2.5$ to $q = 1000$, providing the first remnant models that can be used in the large-mass-ratio regime. As a byproduct of these studies, we also update previous analytical fits for the kick velocities. Such models for the remnant properties may help in developing efficient binary population models, probing high-mass-ratio BBH mergers, and investigating the nature of the remnant black hole using GW data. Our surrogate model is publicly available through the BHPTNR_Remnant Python package.

Finally, we demonstrate how remnant quantities may help in building future NR-calibrated ppBHPT models, particularly in the merger-ringdown regime. Developing a robust framework to incorporate remnant information into the waveform modeling pipeline will be considered in future work.

ACKNOWLEDGMENTS

The authors would like to thank Estuti Shukla for initiating the calculation of remnant properties from ppBHPT waveform data a few years ago (2020). The authors also acknowledge support from NSF Grants No. PHY-2106755 (G. K), No. PHY-2110496 (T. I. and S. F), and DMS-1912716 (T. I., S. F, and G. K). Part of this work is additionally supported by the Heising-Simons Foundation, the Simons Foundation, and NSF Grant Nos. PHY-1748958. Simulations were performed on CARNiE at the Center for Scientific Computing and Visualization Research (CSCVR) of UMassD, which is supported by the ONR/Defense University Research Instrumentation Program (DURIP) Grant No. N00014181255, the UMass-URI UNITY supercomputer supported by the Massachusetts Green High Performance Computing Center (MGHPCC) and ORNL SUMMIT under allocation AST166.

APPENDIX: APPROXIMATING THE ADM MASS

To compute the remnant mass of a nonspinning binary according to Eq. (12), it is important to calculate the ADM

mass of the spacetime. The ADM mass is readily computed in a numerical relativity simulation but unavailable in waveform models. In this appendix, we provide numerical evidence that the ADM mass, as computed in SpEC simulations [29], can be approximated as

$$M_{\rm ADM} \sim M + E_{\rm binding}(t_{\rm initial}), \tag{A1}$$

where $E_{\rm binding}(=-E_0)$ is the post-Newtonian binding energy of the binary at the start of the waveform and $M = m_1 + m_2$ (M is set to unity in a typical NR simulation). This dependency can be understood by noting that there is no gravitational radiation content at the start of an NR simulation. Consequently, the ADM mass as computed in NR will depend only on the initial data (such as the initial coordinate separation of the two black holes) prescribed on the finite computational domain.

To demonstrate this, we select a set of 10 NR simulations for nonspinning BBHs from the SXS catalog [29].[6] For each NR simulation, we extract $M_{\rm ADM}$ from the simulation's metadata file. We then use the initial orbital frequency of the simulation (also taken from the metadata file) to compute $E_{\rm binding}$ using a PN expression (7). In Fig. 10, we show $M_{\rm ADM}$ as well as its approximated value $M + E_{\rm binding}$. We find that $M_{\rm ADM}$ and $M + E_{\rm binding}$ closely match with each other. Small discrepancies appear at larger values of initial orbital frequency, Ω, which is where PN approximations become less reliable. Additional (probably less important) discrepancies may be due to junk radiation content lurking in the initial data and evaluation of the ADM integral on a finite outer boundary [108].

Considering Fig. 10's apparent dependence on q, we note that due to the computational challenges associated with high-mass-ratio NR simulations, available NR waveform durations vary with mass ratio. For example, the $q = 1$ simulation covers $\sim 25,000M$ in duration and has the lowest initial orbital frequency, whereas the $q = 8.72$ simulation only covers $\sim 5000M$ in duration and has the highest initial orbital frequency. When estimating the remnant mass according to Eq. (12), one would use a sufficiently long waveform such that the post-Newtonian binding energy estimated at $t_{\rm initial}$ is accurate.

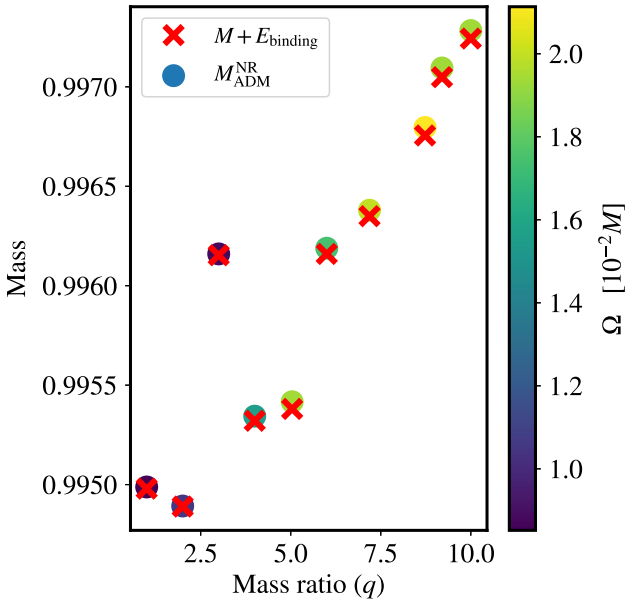

FIG. 10. We demonstrate that the ADM mass of the binary, $M^{\rm NR}_{\rm ADM}$, measured in an NR simulation (circles) can be well approximated by $M + E_{\rm binding}(t = t_{\rm initial})$ (red crosses). The color bar shows the value of the initial orbital frequency, Ω. We see worsening agreement at larger values of Ω, which is where PN approximations become less reliable. Here $t_{\rm initial}$ denotes that we evaluate the PN expression for the binding energy (7) at the start of the simulation.

[6] https://data.black-holes.org/waveforms/catalog.html.

[1] B. P. Abbott *et al.* (LIGO Scientific and Virgo Collaborations), Observation of Gravitational Waves from a Binary Black Hole Merger, Phys. Rev. Lett. **116**, 061102 (2016).

[2] Joan Centrella, John G. Baker, Bernard J. Kelly, and James R. van Meter, Black-hole binaries, gravitational waves, and numerical relativity, Rev. Mod. Phys. **82**, 3069 (2010).

[3] Jose A. Gonzalez, Ulrich Sperhake, Bernd Bruegmann, Mark Hannam, and Sascha Husa, Total Recoil: The Maximum Kick from Nonspinning Black-Hole Binary Inspiral, Phys. Rev. Lett. **98**, 091101 (2007).

[4] F. Herrmann, Ian Hinder, D. Shoemaker, and P. Laguna, Unequal mass binary black hole plunges and gravitational recoil, Classical Quantum Gravity **24**, S1 (2006).

[5] James Healy and Carlos O. Lousto, Ultimate Black Hole Recoil: What the Maximum High Energy Collisions Kick is?, Phys. Rev. Lett. **131**, 071401 (2023).

[6] Asher Peres, Classical radiation recoil, Phys. Rev. **128**, 2471 (1962).

[7] Jacob D. Bekenstein, Gravitational-radiation recoil and runaway black holes, Astrophys. J. **183**, 657 (1973).

[8] Manuela Campanelli, Carlos O. Lousto, Yosef Zlochower, and David Merritt, Maximum Gravitational Recoil, Phys. Rev. Lett. **98**, 231102 (2007).

[9] J. A. Gonzalez, M. D. Hannam, U. Sperhake, Bernd Bruegmann, and S. Husa, Supermassive Recoil Velocities for Binary Black-Hole Mergers with Antialigned Spins, Phys. Rev. Lett. **98**, 231101 (2007).

[10] Carlos O. Lousto and Yosef Zlochower, Hangup Kicks: Still Larger Recoils by Partial Spin/Orbit Alignment of Black-Hole Binaries, Phys. Rev. Lett. **107**, 231102 (2011).
[11] Werner Israel, Event horizons in static electrovac space-times, Commun. Math. Phys. **8**, 245 (1968).
[12] B. Carter, Axisymmetric Black Hole Has Only Two Degrees of Freedom, Phys. Rev. Lett. **26**, 331 (1971).
[13] Vijay Varma, Sylvia Biscoveanu, Tousif Islam, Feroz H. Shaik, Carl-Johan Haster, Maximiliano Isi, Will M. Farr, Scott E. Field, and Salvatore Vitale, Evidence of Large Recoil Velocity from a Black Hole Merger Signal, Phys. Rev. Lett. **128**, 191102 (2022).
[14] Sizheng Ma, Matthew Giesler, Vijay Varma, Mark A. Scheel, and Yanbei Chen, Universal features of gravitational waves emitted by superkick binary black hole systems, Phys. Rev. D **104**, 084003 (2021).
[15] Abhirup Ghosh, Nathan K. Johnson-Mcdaniel, Archisman Ghosh, Chandra Kant Mishra, Parameswaran Ajith, Walter Del Pozzo, Christopher P. L. Berry, Alex B. Nielsen, and Lionel London, Testing general relativity using gravitational wave signals from the inspiral, merger and ringdown of binary black holes, Classical Quantum Gravity **35**, 014002 (2018).
[16] B. P. Abbott *et al.* (LIGO Scientific and Virgo Collaborations), Tests of General Relativity with GW150914, Phys. Rev. Lett. **116**, 221101 (2016); **121**, 129902(E) (2018).
[17] A. sesana, Extreme recoils: Impact on the detection of gravitational waves from massive black hole binaries, Mon. Not. R. Astron. Soc. **382**, L6 (2007).
[18] Alessia Gualandris and David Merritt, Ejection of supermassive black holes from galaxy cores, Astrophys. J. **678**, 780 (2008).
[19] David Merritt, Milos Milosavljevic, Marc Favata, Scott A. Hughes, and Daniel E. Holz, Consequences of gravitational radiation recoil, Astrophys. J. Lett. **607**, L9 (2004).
[20] R. Abbott *et al.* (LIGO Scientific, Virgo, and KAGRA Collaborations), The Population of Merging Compact Binaries Inferred using Gravitational Waves through GWTC-3, Phys. Rev. X **13**, 011048 (2023).
[21] L. A. C. van Son, S. E. de Mink, M. Renzo, S. Justham, E. Zapartas, K. Breivik, T. Callister, W. M. Farr, and C. Conroy, No peaks without valleys: The stable mass transfer channel for gravitational-wave sources in light of the neutron star–black hole mass gap, Astrophys. J. **940**, 184 (2022).
[22] Ethan Payne and Eric Thrane, Model exploration in gravitational-wave astronomy with the maximum population likelihood, Phys. Rev. Res. **5**, 023013 (2023).
[23] Davide Gerosa and Maya Fishbach, Hierarchical mergers of stellar-mass black holes and their gravitational-wave signatures, Nat. Astron. **5**, 749 (2021).
[24] Chase Kimball, Colm Talbot, Christopher P. L. Berry, Matthew Carney, Michael Zevin, Eric Thrane, and Vicky Kalogera, Black hole genealogy: Identifying hierarchical mergers with gravitational waves, Astrophys. J. **900**, 177 (2020).
[25] Carl L. Rodriguez, Michael Zevin, Pau Amaro-Seoane, Sourav Chatterjee, Kyle Kremer, Frederic A. Rasio, and Claire S. Ye, Black holes: The next generation—repeated mergers in dense star clusters and their gravitational-wave properties, Phys. Rev. D **100**, 043027 (2019).
[26] Maya Fishbach, Daniel E. Holz, and Ben Farr, Are LIGO's black holes made from smaller black holes?, Astrophys. J. Lett. **840**, L24 (2017).
[27] Davide Gerosa and Emanuele Berti, Are merging black holes born from stellar collapse or previous mergers?, Phys. Rev. D **95**, 124046 (2017).
[28] M. Coleman Miller and Douglas P. Hamilton, Production of intermediate-mass black holes in globular clusters, Mon. Not. R. Astron. Soc. **330**, 232 (2002).
[29] Michael Boyle, Daniel Hemberger, Dante A. B. Iozzo, Geoffrey Lovelace, Serguei Ossokine, Harald P. Pfeiffer, Mark A. Scheel, Leo C. Stein, Charles J. Woodford, Aaron B. Zimmerman *et al.*, The SXS collaboration catalog of binary black hole simulations, Classical Quantum Gravity **36**, 195006 (2019).
[30] Alejandro Bohé *et al.*, Improved effective-one-body model of spinning, nonprecessing binary black holes for the era of gravitational-wave astrophysics with advanced detectors, Phys. Rev. D **95**, 044028 (2017).
[31] Roberto Cotesta, Alessandra Buonanno, Alejandro Bohé, Andrea Taracchini, Ian Hinder, and Serguei Ossokine, Enriching the symphony of gravitational waves from binary black holes by tuning higher harmonics, Phys. Rev. D **98**, 084028 (2018).
[32] Roberto Cotesta, Sylvain Marsat, and Michael Pürrer, Frequency domain reduced order model of aligned-spin effective-one-body waveforms with higher-order modes, Phys. Rev. D **101**, 124040 (2020).
[33] Yi Pan, Alessandra Buonanno, Andrea Taracchini, Lawrence E. Kidder, Abdul H. Mroué, Harald P. Pfeiffer, Mark A. Scheel, and Béla Szilágyi, Inspiral-merger-ringdown waveforms of spinning, precessing black-hole binaries in the effective-one-body formalism, Phys. Rev. D **89**, 084006 (2014).
[34] Stanislav Babak, Andrea Taracchini, and Alessandra Buonanno, Validating the effective-one-body model of spinning, precessing binary black holes against numerical relativity, Phys. Rev. D **95**, 024010 (2017).
[35] Alessandro Nagar, James Healy, Carlos O. Lousto, Sebastiano Bernuzzi, and Angelica Albertini, Numerical-relativity validation of effective-one-body waveforms in the intermediate-mass-ratio regime, Phys. Rev. D **105**, 124061 (2022).
[36] Sascha Husa, Sebastian Khan, Mark Hannam, Michael Pürrer, Frank Ohme, Xisco Jiménez Forteza, and Alejandro Bohé, Frequency-domain gravitational waves from nonprecessing black-hole binaries. I. New numerical waveforms and anatomy of the signal, Phys. Rev. D **93**, 044006 (2016).
[37] Sebastian Khan, Sascha Husa, Mark Hannam, Frank Ohme, Michael Pürrer, Xisco Jiménez Forteza, and Alejandro Bohé, Frequency-domain gravitational waves from nonprecessing black-hole binaries. II. A phenomenological model for the advanced detector era, Phys. Rev. D **93**, 044007 (2016).
[38] Lionel London, Sebastian Khan, Edward Fauchon-Jones, Cecilio García, Mark Hannam, Sascha Husa, Xisco Jiménez-Forteza, Chinmay Kalaghatgi, Frank Ohme, and

Francesco Pannarale, First Higher-Multipole Model of Gravitational Waves from Spinning and Coalescing Black-Hole Binaries, Phys. Rev. Lett. **120**, 161102 (2018).
[39] Sebastian Khan, Katerina Chatziioannou, Mark Hannam, and Frank Ohme, Phenomenological model for the gravitational-wave signal from precessing binary black holes with two-spin effects, Phys. Rev. D **100**, 024059 (2019).
[40] Sebastian Khan, Frank Ohme, Katerina Chatziioannou, and Mark Hannam, Including higher order multipoles in gravitational-wave models for precessing binary black holes, Phys. Rev. D **101**, 024056 (2020).
[41] Geraint Pratten *et al.*, Computationally efficient models for the dominant and subdominant harmonic modes of precessing binary black holes, Phys. Rev. D **103**, 104056 (2021).
[42] Héctor Estellés, Antoni Ramos-Buades, Sascha Husa, Cecilio García-Quirós, Marta Colleoni, Leïla Haegel, and Rafel Jaume, Phenomenological time domain model for dominant quadrupole gravitational wave signal of coalescing binary black holes, Phys. Rev. D **103**, 124060 (2021).
[43] Héctor Estellés, Sascha Husa, Marta Colleoni, David Keitel, Maite Mateu-Lucena, Cecilio García-Quirós, Antoni Ramos-Buades, and Angela Borchers, Time-domain phenomenological model of gravitational-wave subdominant harmonics for quasicircular nonprecessing binary black hole coalescences, Phys. Rev. D **105**, 084039 (2022).
[44] Héctor Estellés, Marta Colleoni, Cecilio García-Quirós, Sascha Husa, David Keitel, Maite Mateu-Lucena, Maria de Lluc Planas, and Antoni Ramos-Buades, New twists in compact binary waveform modeling: A fast time-domain model for precession, Phys. Rev. D **105**, 084040 (2022).
[45] Eleanor Hamilton, Lionel London, Jonathan E. Thompson, Edward Fauchon-Jones, Mark Hannam, Chinmay Kalaghatgi, Sebastian Khan, Francesco Pannarale, and Alex Vano-Vinuales, Model of gravitational waves from precessing black-hole binaries through merger and ringdown, Phys. Rev. D **104**, 124027 (2021).
[46] Jonathan Blackman, Scott E. Field, Chad R. Galley, Béla Szilágyi, Mark A. Scheel, Manuel Tiglio, and Daniel A. Hemberger, Fast and Accurate Prediction of Numerical Relativity Waveforms from Binary Black Hole Coalescences Using Surrogate Models, Phys. Rev. Lett. **115**, 121102 (2015).
[47] Jonathan Blackman, Scott E. Field, Mark A. Scheel, Chad R. Galley, Christian D. Ott, Michael Boyle, Lawrence E. Kidder, Harald P. Pfeiffer, and Béla Szilágyi, Numerical relativity waveform surrogate model for generically precessing binary black hole mergers, Phys. Rev. D **96**, 024058 (2017).
[48] Jonathan Blackman, Scott E. Field, Mark A. Scheel, Chad R. Galley, Daniel A. Hemberger, Patricia Schmidt, and Rory Smith, A surrogate model of gravitational waveforms from numerical relativity simulations of precessing binary black hole mergers, Phys. Rev. D **95**, 104023 (2017).
[49] Vijay Varma, Scott E. Field, Mark A. Scheel, Jonathan Blackman, Lawrence E. Kidder, and Harald P. Pfeiffer, Surrogate model of hybridized numerical relativity binary black hole waveforms, Phys. Rev. D **99**, 064045 (2019).
[50] Vijay Varma, Scott E. Field, Mark A. Scheel, Jonathan Blackman, Davide Gerosa, Leo C. Stein, Lawrence E. Kidder, and Harald P. Pfeiffer, Surrogate models for precessing binary black hole simulations with unequal masses, Phys. Rev. Res. **1**, 033015 (2019).
[51] Tousif Islam, Vijay Varma, Jackie Lodman, Scott E. Field, Gaurav Khanna, Mark A. Scheel, Harald P. Pfeiffer, Davide Gerosa, and Lawrence E. Kidder, Eccentric binary black hole surrogate models for the gravitational waveform and remnant properties: Comparable mass, nonspinning case, Phys. Rev. D **103**, 064022 (2021).
[52] Jooheon Yoo, Vijay Varma, Matthew Giesler, Mark A. Scheel, Carl-Johan Haster, Harald P. Pfeiffer, Lawrence E. Kidder, and Michael Boyle, Targeted large mass ratio numerical relativity surrogate waveform model for GW190814, Phys. Rev. D **106**, 044001 (2022).
[53] Frank Herrmann, Ian Hinder, Deirdre M. Shoemaker, Pablo Laguna, and Richard A. Matzner, Binary black holes: Spin dynamics and gravitational recoil, Phys. Rev. D **76**, 084032 (2007).
[54] Manuela Campanelli, Carlos O. Lousto, Yosef Zlochower, and David Merritt, Large merger recoils and spin flips from generic black-hole binaries, Astrophys. J. Lett. **659**, L5 (2007).
[55] Luciano Rezzolla, Enrico Barausse, Ernst Nils Dorband, Denis Pollney, Christian Reisswig, Jennifer Seiler, and Sascha Husa, On the final spin from the coalescence of two black holes, Phys. Rev. D **78**, 044002 (2008).
[56] Luciano Rezzolla, Peter Diener, Ernst Nils Dorband, Denis Pollney, Christian Reisswig, Erik Schnetter, and Jennifer Seiler, The final spin from the coalescence of aligned-spin black-hole binaries, Astrophys. J. Lett. **674**, L29 (2008).
[57] Michael Kesden, Can binary mergers produce maximally spinning black holes?, Phys. Rev. D **78**, 084030 (2008).
[58] Wolfgang Tichy and Pedro Marronetti, The final mass and spin of black hole mergers, Phys. Rev. D **78**, 081501 (2008).
[59] Carlos O. Lousto and Yosef Zlochower, Further insight into gravitational recoil, Phys. Rev. D **77**, 044028 (2008).
[60] Enrico Barausse and Luciano Rezzolla, Predicting the direction of the final spin from the coalescence of two black holes, Astrophys. J. Lett. **704**, L40 (2009).
[61] Enrico Barausse, Viktoriya Morozova, and Luciano Rezzolla, On the mass radiated by coalescing black-hole binaries, Astrophys. J. **758**, 63 (2012); **786**, 76(E) (2014).
[62] Carlos O. Lousto, Yosef Zlochower, Massimo Dotti, and Marta Volonteri, Gravitational recoil from accretion-aligned black-hole binaries, Phys. Rev. D **85**, 084015 (2012).
[63] Carlos O. Lousto and Yosef Zlochower, Nonlinear gravitational recoil from the mergers of precessing black-hole binaries, Phys. Rev. D **87**, 084027 (2013).
[64] James Healy, Carlos O. Lousto, and Yosef Zlochower, Remnant mass, spin, and recoil from spin aligned black-hole binaries, Phys. Rev. D **90**, 104004 (2014).
[65] Yosef Zlochower and Carlos O. Lousto, Modeling the remnant mass, spin, and recoil from unequal-mass, precessing black-hole binaries: The intermediate mass ratio regime, Phys. Rev. D **92**, 024022 (2015); **94**, 029901(E) (2016).

[66] Fabian Hofmann, Enrico Barausse, and Luciano Rezzolla, The final spin from binary black holes in quasi-circular orbits, Astrophys. J. Lett. **825**, L19 (2016).
[67] Davide Gerosa and Michael Kesden, PRECESSION: Dynamics of spinning black-hole binaries with Python, Phys. Rev. D **93**, 124066 (2016).
[68] James Healy and Carlos O. Lousto, Remnant of binary black-hole mergers: New simulations and peak luminosity studies, Phys. Rev. D **95**, 024037 (2017).
[69] James Healy and Carlos O. Lousto, Hangup effect in unequal mass binary black hole mergers and further studies of their gravitational radiation and remnant properties, Phys. Rev. D **97**, 084002 (2018).
[70] Pranesh A. Sundararajan, Gaurav Khanna, and Scott A. Hughes, Binary black hole merger gravitational waves and recoil in the large mass ratio limit, Phys. Rev. D **81**, 104009 (2010).
[71] Davide Gerosa, François Hébert, and Leo C. Stein, Black-hole kicks from numerical-relativity surrogate models, Phys. Rev. D **97**, 104049 (2018).
[72] Leïla Haegel and Sascha Husa, Predicting the properties of black-hole merger remnants with deep neural networks, Classical Quantum Gravity **37**, 135005 (2020).
[73] David Keitel *et al.*, The most powerful astrophysical events: Gravitational-wave peak luminosity of binary black holes as predicted by numerical relativity, Phys. Rev. D **96**, 024006 (2017).
[74] Xisco Jiménez-Forteza, David Keitel, Sascha Husa, Mark Hannam, Sebastian Khan, and Michael Pürrer, Hierarchical data-driven approach to fitting numerical relativity data for nonprecessing binary black holes with an application to final spin and radiated energy, Phys. Rev. D **95**, 064024 (2017).
[75] Vijay Varma, Davide Gerosa, Leo C. Stein, François Hébert, and Hao Zhang, High-Accuracy Mass, Spin, and Recoil Predictions of Generic Black-Hole Merger Remnants, Phys. Rev. Lett. **122**, 011101 (2019).
[76] Afura Taylor and Vijay Varma, Gravitational wave peak luminosity model for precessing binary black holes, Phys. Rev. D **102**, 104047 (2020).
[77] Carlos O. Lousto and James Healy, Exploring the Small Mass Ratio Binary Black Hole Merger via Zeno's Dichotomy Approach, Phys. Rev. Lett. **125**, 191102 (2020).
[78] Carlos O. Lousto and James Healy, Study of the intermediate mass ratio black hole binary merger up to 1000:1 with numerical relativity, Classical Quantum Gravity **40**, 09LT01 (2023).
[79] Matthew Giesler, Mark A. Scheel, and Saul A. Teukolsky, Numerical simulations of extreme mass ratio binary black holes (to be published).
[80] Tousif Islam, Scott E. Field, Scott A. Hughes, Gaurav Khanna, Vijay Varma, Matthew Giesler, Mark A. Scheel, Lawrence E. Kidder, and Harald P. Pfeiffer, Surrogate model for gravitational wave signals from nonspinning, comparable-to large-mass-ratio black hole binaries built on black hole perturbation theory waveforms calibrated to numerical relativity, Phys. Rev. D **106**, 104025 (2022).
[81] Nur E. M. Rifat, Scott E. Field, Gaurav Khanna, and Vijay Varma, Surrogate model for gravitational wave signals from comparable and large-mass-ratio black hole binaries, Phys. Rev. D **101**, 081502 (2020).
[82] Jonathan Blackman, Scott Field, Chad Galley, and Vijay Varma, gwsurrogate, https://pypi.python.org/pypi/gwsurrogate/.
[83] Scott E Field, Chad R Galley, Jan S Hesthaven, Jason Kaye, and Manuel Tiglio, Fast Prediction and Evaluation of Gravitational Waveforms using Surrogate Models, Phys. Rev. X **4**, 031006 (2014).
[84] Scott Field, Tousif Islam, Gaurav Khanna, Nur Rifat, and Vijay Varma, BHPTNRSurrogate, http://bhptoolkit.org/BHPTNRSurrogate/.
[85] Black Hole Perturbation Toolkit, bhptoolkit.org.
[86] Pranesh A. Sundararajan, Gaurav Khanna, and Scott A. Hughes, Towards adiabatic waveforms for inspiral into Kerr black holes. I. A New model of the source for the time domain perturbation equation, Phys. Rev. D **76**, 104005 (2007).
[87] Pranesh A. Sundararajan, Gaurav Khanna, Scott A. Hughes, and Steve Drasco, Towards adiabatic waveforms for inspiral into Kerr black holes: II. Dynamical sources and generic orbits, Phys. Rev. D **78**, 024022 (2008).
[88] Anil Zenginoglu and Gaurav Khanna, Null Infinity Waveforms from Extreme-Mass-Ratio Inspirals in Kerr Spacetime, Phys. Rev. X **1**, 021017 (2011).
[89] Tousif Islam, Interplay between numerical-relativity and black hole perturbation theory in the intermediate-mass-ratio regime, Phys. Rev. D **108**, 044013 (2023).
[90] Tousif Islam and Gaurav Khanna, On the approximate relation between black-hole perturbation theory and numerical relativity, arXiv:2307.03155.
[91] Kip S. Thorne, Multipole expansions of gravitational radiation, Rev. Mod. Phys. **52**, 299 (1980).
[92] Carlos O. Lousto and Yosef Zlochower, A practical formula for the radiated angular momentum, Phys. Rev. D **76**, 041502 (2007).
[93] Milton Ruiz, Ryoji Takahashi, Miguel Alcubierre, and Dario Nunez, Multipole expansions for energy and momenta carried by gravitational waves, Gen. Relativ. Gravit. **40**, 2467 (2008).
[94] Tousif Islam, Scott Field, and Gaurav Khanna, GW_remnant, https://pypi.org/project/gw-remnant/.
[95] Alexandre Le Tiec, Luc Blanchet, and Bernard F. Whiting, The first law of binary black hole mechanics in general relativity and post-Newtonian theory, Phys. Rev. D **85**, 064039 (2012).
[96] Richard L. Arnowitt, Stanley Deser, and Charles W. Misner, The dynamics of general relativity, Gen. Relativ. Gravit. **40**, 1997 (2008).
[97] Abhay Ashtekar and Anne Magnon-Ashtekar, Energy-Momentum in General Relativity, Phys. Rev. Lett. **43**, 181 (1979).
[98] Béla Szilágyi, Jonathan Blackman, Alessandra Buonanno, Andrea Taracchini, Harald P. Pfeiffer, Mark A. Scheel, Tony Chu, Lawrence E Kidder, and Yi Pan, Approaching the Post-Newtonian Regime with Numerical Relativity: A Compact-Object Binary Simulation Spanning 350 Gravitational-Wave Cycles, Phys. Rev. Lett. **115**, 031102 (2015).

[99] Miren Radia, Ulrich Sperhake, Emanuele Berti, and Robin Croft, Anomalies in the gravitational recoil of eccentric black-hole mergers with unequal mass ratios, Phys. Rev. D **103**, 104006 (2021).

[100] Carl Edward Rasmussen, Gaussian processes in machine learning, in *Advanced Lectures on Machine Learning: ML Summer Schools 2003, Canberra, Australia, 2003, Tübingen, Germany, 2003, Revised Lectures*, edited by Olivier Bousquet, Ulrike von Luxburg, and Gunnar Rätsch (Springer, Berlin, Heidelberg, 2004), pp. 63–71.

[101] F. Pedregosa, G. Varoquaux, A. Gramfort, V. Michel, B. Thirion, O. Grisel, M. Blondel, P. Prettenhofer, R. Weiss, V. Dubourg, J. Vanderplas, A. Passos, D. Cournapeau, M. Brucher, M. Perrot, and E. Duchesnay, Scikit-learn: Machine learning in Python, J. Mach. Learn. Res. **12**, 2825 (2011), https://www.jmlr.org/papers/v12/pedregosa11a.html.

[102] Roberto Cotesta, Sylvain Marsat, and Michael Pürrer, Frequency domain reduced order model of aligned-spin effective-one-body waveforms with higher-order modes, Phys. Rev. D **101**, 124040 (2020).

[103] Dante AB Iozzo, Neev Khera, Leo C Stein, Keefe Mitman, Michael Boyle, Nils Deppe, François Hébert, Lawrence E Kidder, Jordan Moxon, Harald P Pfeiffer *et al.*, Comparing remnant properties from horizon data and asymptotic data in numerical relativity, Phys. Rev. D **103**, 124029 (2021).

[104] Tousif Islam, Scott Field, and Gaurav Khanna, BHPTNRremnant, https://pypi.org/project/BHPTNRremnant.

[105] Pauli Virtanen *et al.* (SciPy 1.0 Contributors), SciPy 1.0: Fundamental Algorithms for Scientific Computing in Python, Nat. Methods **17**, 261 (2020).

[106] Marc Favata, Scott A. Hughes, and Daniel E. Holz, How black holes get their kicks: Gravitational radiation recoil revisited, Astrophys. J. Lett. **607**, L5 (2004).

[107] Walter Rudin, Real and complex analysis, in *Real and Complex Analysis* (McGraw-Hill, New York, 1987), p. 40.

[108] Geoffrey Lovelace, Reducing spurious gravitational radiation in binary-black-hole simulations by using conformally curved initial data, Classical Quantum Gravity **26**, 114002 (2009).